J. Adv. Model. Earth Syst., **Vol. 1**, Art. #16, 13 pp.

The Tropical Marine Boundary Layer Under a Deep Convection System: a Large-Eddy Simulation Study

Chin-Hoh Moeng[1], Margaret A. LeMone[1], Marat F. Khairoutdinov[2], Steve K. Krueger[3], Peter A. Bogenschutz[3] and David A. Randall[4]

[1] Mesoscale & Microscale Meteorology Division, National Center for Atmospheric Research[1], Boulder, Colorado
[2] School of Marine and Atmospheric Sciences, Stony Brook University, Stony Brook, New York
[3] Department of Atmospheric Sciences, University of Utah, Salt Lake City, Utah
[4] Department of Atmospheric Science, Colorado State University, Fort Collins, Colorado

Manuscript submitted 1 July 2009; revised 15 October 2009

The tropical marine PBL under the influence of a deep convection system is investigated using a large-domain LES that resolves a wide range of scales, from mesoscale cloud clusters down to energy-containing turbulence. The simulated PBL is dominated by both turbulence and cloud-induced cold-pools. The variance of vertical velocity in the PBL resides mostly in the turbulence scales while that of water vapor mixing ratio resides mostly at the cold-pool scales; however, both turbulence and cold-pool scales contribute about equally to their covariance. The broad scale range of the LES flow field is decomposed into the filtered (i.e., cloud system) and the subfilter (i.e., small convection and turbulence) components using a Gaussian filter with various filter widths. Such decomposed flow fields are used to retrieve information of spatial distribution of the subfilter-scale fluxes and their relationship to the filtered field. This information is then used to evaluate the performance of an eddy-viscosity model commonly used in cloud-resolving models. The subfilter-scale fluxes computed from the eddy-viscosity model correlate reasonably with those retrieved from the LES in the lower cloud layer but not in the PBL; the correlation coefficients between the modeled and the retrieved fluxes are about 0.5 in the lower cloud layer but smaller than 0.2 in the PBL.

DOI:10.3894/JAMES.2009.1.16

1. Introduction

The tropical marine PBL under a deep convection system serves as a medium that transfers heat and moisture from the underlying ocean surface to the convection system, and thus plays a crucial role in determining the cloud evolution and statistics. This PBL regime has been studied by several tropical field experiments [e.g., Line Islands, Barbados Oceanographic and Meteorological Experiment, GARP (Global Atmospheric Research Program) Atlantic Tropical Experiment, GATE, and TOGA-COARE (Tropical Oceans Global Atmosphere-Coupled Ocean-Atmosphere Research Experiment)] as reported by Zipser (1969), Garstang and Betts (1974), Betts (1976), Zipser (1977), Fitzjarrald and Garstang (1981), Johnson and Nicholls (1983), Nicholls and Johnson (1984), Young et al. (1995), Geldmeier and Barnes (1997), and Williams et al. (1996). A clear picture emerges from these studies: The tropical marine PBL is strongly influenced by precipitating convection and associated sub-saturated mesoscale cold pools. Inside cold pools, the PBL air is significantly colder, drier, and windier than that outside, and the surface sensible and latent heat fluxes are much stronger. Cold pools are often referred to as wakes, being left behind from precipitating clouds. A typical wake sounding shows a shallow (or no) mixed layer, topped by a strong temperature inversion (Zipser 1977). It may take several hours for the PBL to recover to its pre-storm condition (Johnson 1981, Barnes and Garstang 1982, Young et al. 1995, Geldmeier and Barnes 1997). These observations indicate that the tropical marine PBL is highly heterogeneous and can differ significantly from the most-studied horizontally homogeneous PBLs.

The purposes of this study are to (1) examine a simulated marine PBL from a large-domain large-eddy simulation (LES) of a tropical convection system and compare it to field observations and (2) demonstrate that the LES can serve as a benchmark to evaluate or develop PBL schemes

[1] NCAR is sponsored by the National Science Foundation

To whom correspondence should be addressed.
Dr. Chin-Hoh Moeng, MMM Division, NCAR, P.O. Box 3000, Boulder, CO 80307-3000, USA
moeng@ucar.edu

for Cloud Resolving Models (CRMs). A typical CRM's horizontal grid mesh is about 1–4 km (Krueger 1988, Weisman et al. 1997, Grabowski et al. 1998, Redelsperger et al. 2000)—too coarse to resolve turbulent motions, which are typically smaller than ~ 1 km. To parameterize the turbulent fluxes, most 3D CRMs adopt the Smagorinsky-Deardorff-type eddy-diffusivity subgrid-scale (SGS) model (Klemp and Wilhelmson 1978, Tao and Soong 1986, Redelsperger and Sommeria 1986, Khairoutdinov and Randall 2003, Bryan et al. 2003). The Smagorinsky-Deardorff-type SGS model was designed for LESs to parameterize just the inertial-subrange part of turbulent motions; how it represents the entire range of turbulent motions in CRMs has not been examined in detail.

The adequacy of a typical horizontal grid size in 3D CRMs in simulating the statistical properties of a squall line system was examined by Bryan et al. (2003). They compared runs with horizontal grid sizes ranging between 1 km to 125 m for a mid-latitude squall line case and found that the statisical properties of the simulated system are not converged even between the runs with 250 m and 125 m grid meshes. Their study suggested that the turbulence is not properly represented in their CRM. In contrast, Khairoutdinov and Randall (2006) demonstrated little difference in the details of the transition between the runs with 100 m and 250 m horizontal resolutions in their high-resolution simulations of the shallow-to-deep convection transition over Amazonia. The grid resolution issue and the role of turbulence may be case dependent.

To examine turbulence representation in CRMs, we performed a LES that covers a numerical domain (~ 205 km × 205 km × 27 km) large enough to resolve a tropical convective system; it also used a grid mesh fine enough to resolve important turbulent eddies (i.e., the energy-containing eddies that are responsible for most of the turbulent transport). The grid mesh is 100 m in x and y and varys from 50 m (in the lowest 1 km) to 150 m in z. The total number of grid points is 2048 × 2048 × 256, about 10^9. The initial sounding and the prescribed large-scale forcing (shown in Fig. 1) are based on an idealized (time averaged) GATE conditions. The mean wind is weak near the surface, but the shear is significant higher up. The sea surface temperature is set to 299.88 K and the sea level pressure 1012 mb. The simulation was initiated by applying small random perturbations to the initial temperature sounding at the lowest grid level. No cold pools or thermal bubbles were required to initiate the convection. The deep convection system reaches a quasi-steady state with its large-scale environment during the last 12 hours of the 24-hour simulation period. The overall cloud evolution and statistics are summarized and reported in a companion paper by Khairoutdinov et al. (2009).

The motivation for performing this computationally intensive LES is to study subgrid-scale (SGS) processes in a typical CRM where the grid size is too coarse to resolve turbulence and small convection. Improving SGS representations in CRMs is one of the research objectives at the NSF Science and Technology Center for Multiscale Modeling of Atmospheric Processes (CMMAP). The aspects of SGS physics may differ in CRMs and climate models. In a climate model all convective motions (deep, shallow clouds and turbulence) are SGS processes and are parameterized separately in terms of the resolvable large-scale flow fields. In a CRM, SGS processes are parameterized in terms of resolvable cloud-scale motions, and hence the relationship between small (the SGS) and large (the resolvable) convection is the key to formulating its SGS parameterizations. Furthermore, the resolvable and the SGS motions in CRMs likely do not have scale separation as often assumed in climate models. Thus, the ensemble-mean closure concept used to parameterize SGS processes in climate models may be improper in representing SGS processes in CRMs.

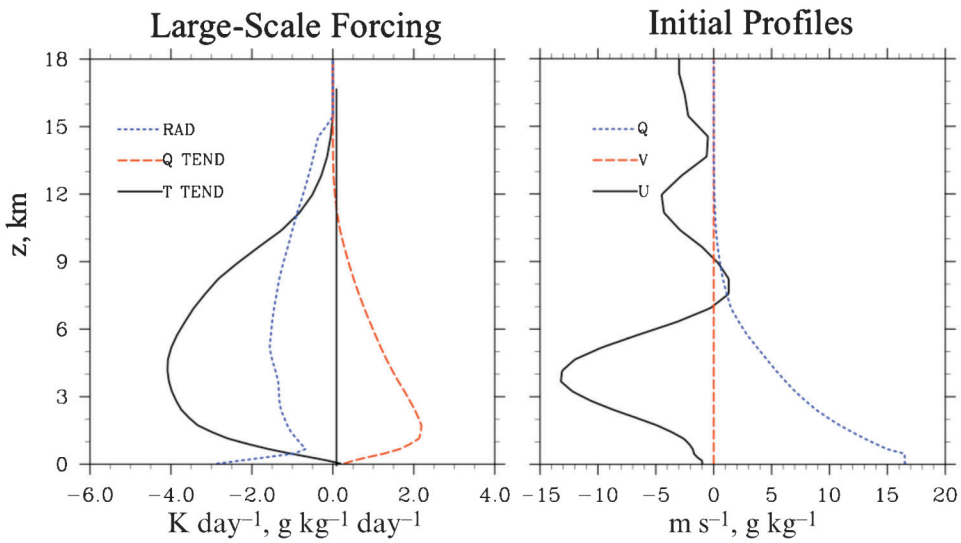

Figure 1. Initial sounding and prescribed large-scale forcing for the LES.

In this study, we focus only on the lowest kilometer of the convective system, which includes the PBL and the lower cloud layer, and the relationship between turbulence and cloud-system scales. The analysis and conclusions in this paper are based on one instantaneous flow field of the LES near the end of the 24-hour simulation time but we also checked the robustness of our conclusions from different time periods of the LES flow fields. The characteristics of the simulated PBL are shown in section 2; the range of scales that are explicitly calculated by the LES is given in section 3 from a spectral analysis; a scale separation of turbulence (subfilter scales) from the cloud-system scales (filterscales) is performed in section 4; and the horizontal distributions of the subfilter-scale fluxes, with various filter widths, are retrieved in section 5.1. These filter- and subfilter-scales fields can be viewed as the resolvable and SGS fields in a CRM, respectively, and the filter width corresponds to the horizontal grid resolution (which may be 4∼6 times of the grid size depending on numerical schemes) of a CRM. The retrieved filtered and subfilter fields are then used to evaluate the Smagorinsky-Deardorff eddy-diffusivity SGS model commonly used in CRMs (section 5.2) as an example to show how the LES can serve as a benchmark for testing and developing SGS models for CRMs. Section 6 presents our summary and conclusions.

2. Characteristics of the simulated PBL

The spatial distributions of potential temperature θ, water vapor mixing ratio q, and horizontal wind speed $\sqrt{u^2+v^2}$ at the first grid level ($z = 25$ m), along with the vertically integrated condensed water (liquid and ice) mixing ratio, near the end of the 24-hour simulation time, are shown in Fig. 2. The most distinct features are the cold pools of various sizes. Their sizes, much larger than turbulence scales, range from a few kilometers to several tens of kilometers in diameter depending on the size and the stage of life cycle of the cloud system generating the cold pool and how much the cold pool has been modified by surface fluxes. These cold pools consist of drier and windier air, as observed (e.g., Johnson 1981, Young et al. 1995, Geldmeier and Barnes 1997, Jorgensen et al. 1997). On average, the air inside the cold pools is 2–3 K colder and 3–4 g kg^{-1} drier than that outside (Figs. 2a and 2b). These cold pools are fed by downdrafts from precipitating convective systems, which then spread outward as density currents and slowly recover to pre-storm conditions. The high wind areas (Fig. 2c) represent the outward spreading of density currents, which enlarges the cold pools throughout the recovering stage. The recovering (i.e., outward spreading) time of the simulated cold pools ranges from 2 to 6 hours, based on a video showing the time evolution of the near-surface potential temperature field.

Vertical cross sections (along y ∼ 90 km) of θ, q, u (the x-component of wind), and the vertical velocity w in the lowest 500 m are given in Fig. 3. This vertical cross section cuts through a recovering cold pool located at about 100 km$< x <$160 km where the sky is almost clear as indicated by Fig. 2d. Relative to its surrounding air, the cold pool is coldest near the surface, but the dry air is still being carried downward from above. The dry air is brought down in unsaturated downdrafts (Fig. 3d), which diverge near the surface as low-level outflow (Fig. 3c).

The colder, drier and windier air near the surface produces much larger surface fluxes of temperature, moisture and momentum inside cold pools than outside. The surface fluxes shown in Fig. 4, computed based on surface similarity theory, are highly heterogeneous; they are much larger inside cold pools. The horizontal averages of the heat and moisture fluxes over the entire numerical domain (at this simulation time) are only about 12 W m^{-2} and 54 W m^{-2}, respectively. (Here, the warm colors indicate regions where the fluxes are larger than the horizontal mean and the cold colors for those smaller than the mean.)

To compare the PBL statistics inside and outside of cold pools, we performed a conditional sampling by choosing a cold-pool subdomain (80 km$<$ x $<$100 km and 150 km$<$ y $<$170 km) and a subdomain outside of cold pools (180 km$<$ x $<$200 km and 180 km$<$ y $<$200 km), which are marked in Fig. 4b. Their statistics, shown in Figs. 5 and 6, were computed by averaging over each of these 20 km × 20 km subdomains, with the dash-dot curves representing the cold-pool subdomain, the dotted curves for the outside-cold-pool subdomain. We also show the statistics averaged over the entire numerical domain in solid curves. (Note that the data sample of 20 km × 20 km used for this averaging is much larger than that of a typical PBL LES where averaging is usually obtained from an area of about 5 km × 5 km.)

The mean vertical velocity inside the cold pool is negative, indicating the cold-pool-induced subsidence evidenced in Fig. 3d. From the mean Θ profile, we may estimate the PBL heights: it is only about 75 m inside the cold pool and about 200–300 m outside. (Thus, we acknowldge that the grid resolution of this LES may not be fine enough to well resolve the energy-containing eddies in these shallow PBLs; nonetheless, this large-domain LES already pushed the limit of our computer resources.) The temperature above the shallow PBL in the cold-pool subdomain is strongly stably stratified, which agrees with the observations of strong capping inversions over cold pools (e.g., Zipser 1977). Both the strong inversion and mean subsidence act to suppress the growth of the PBL and lead to a shallow mixed layer in the cold-pool subdomain. The mean q decreases significantly with height in the cold-pool area, due to the continued dry air pushed down from above the cold pool. In the outside-cold-pool subdomain, the moisture and temperature in the PBL are more well mixed. Note that the PBL in this selected outside-cold-pool subdomain is rather shallow compared to the observed fair-weather PBL (e.g., Nicholls and LeMone 1980) but as indicated in Fig. 2d there are clouds in this subdomain so it may not compare directly to the observed fair-weather PBL.

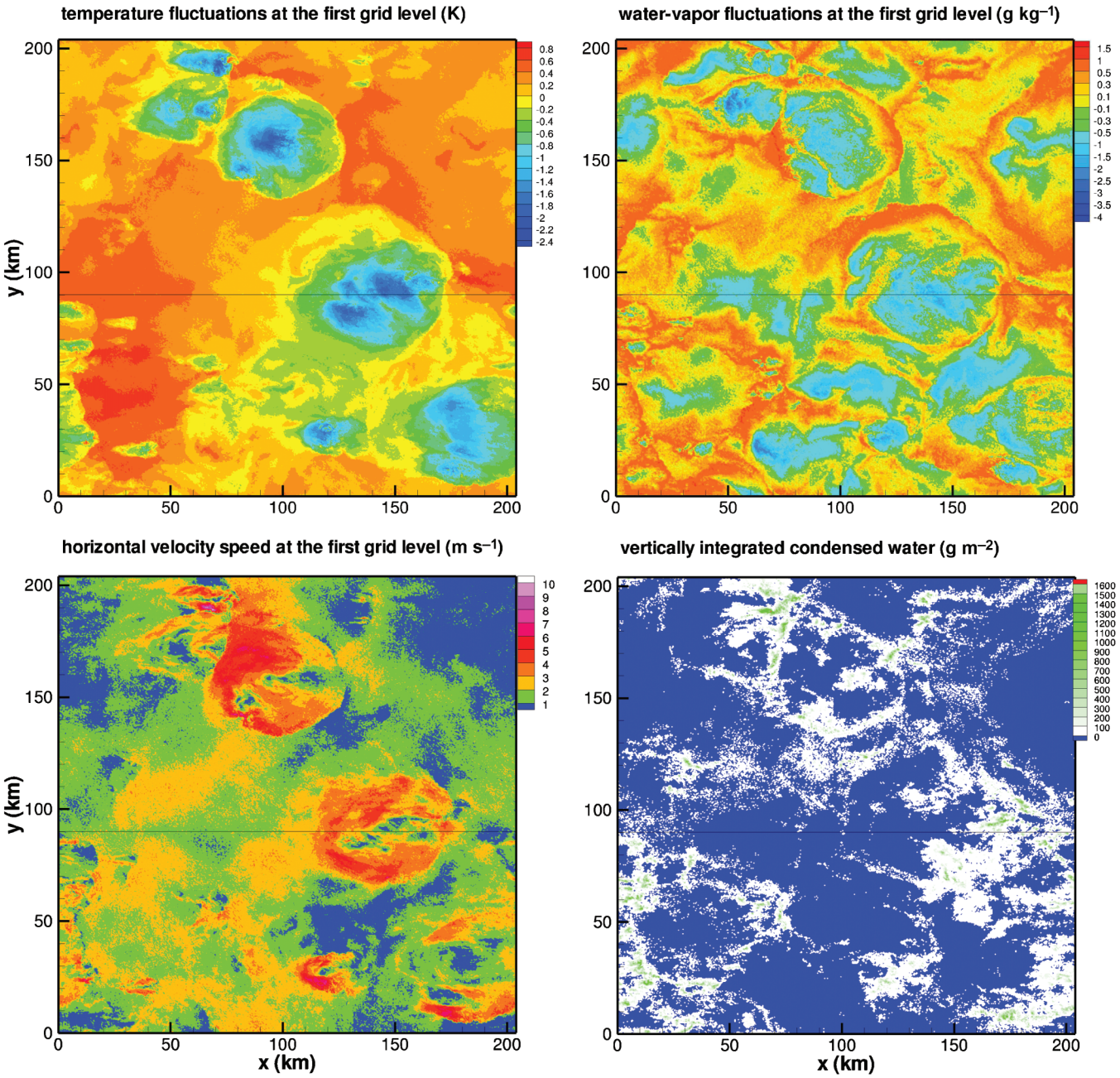

Figure 2. Potential temperature, water vapor mixing ratio, and horizontal wind speed at the z = 25 m, and the vertically integrated condensed water (lower-right) from the LES. The solid line shows a reference line across y = 90 km.

Figure 6 shows the profiles of the vertical fluxes of potential temperature and water vapor for the two subdomains and for the entire domain. The subdomain fluxes are computed as mean correlations of the w and θ (or q) fluctuations deviating from the horizontal averages over each subdomain. Fluxes shown here thus include only the resolvable-scale contributions. (The surface fluxes are computed as subdomain averages from Fig. 4.) The sensible heat flux is small particularly outside of cold pools, which is typical for tropical oceans in undisturbed conditions (e.g., Nicholls and LeMone 1980). The moisture flux over the cold-pool subdomain decreases sharply with height, suggesting a significant moistening process (due to flux convergence) of the PBL. The temperature flux profile also shows a larger flux convergence in the PBL over the cold-pool subdomain, compared to that outside. The moistening and warming trend signifies the recovery process of the cold pool.

It is difficult to define the mean cloud base height. Figure 7 shows the time evolution of the horizontally averaged non-precipitating condensed water amount and the turbulence kinetic energy (TKE) during the last

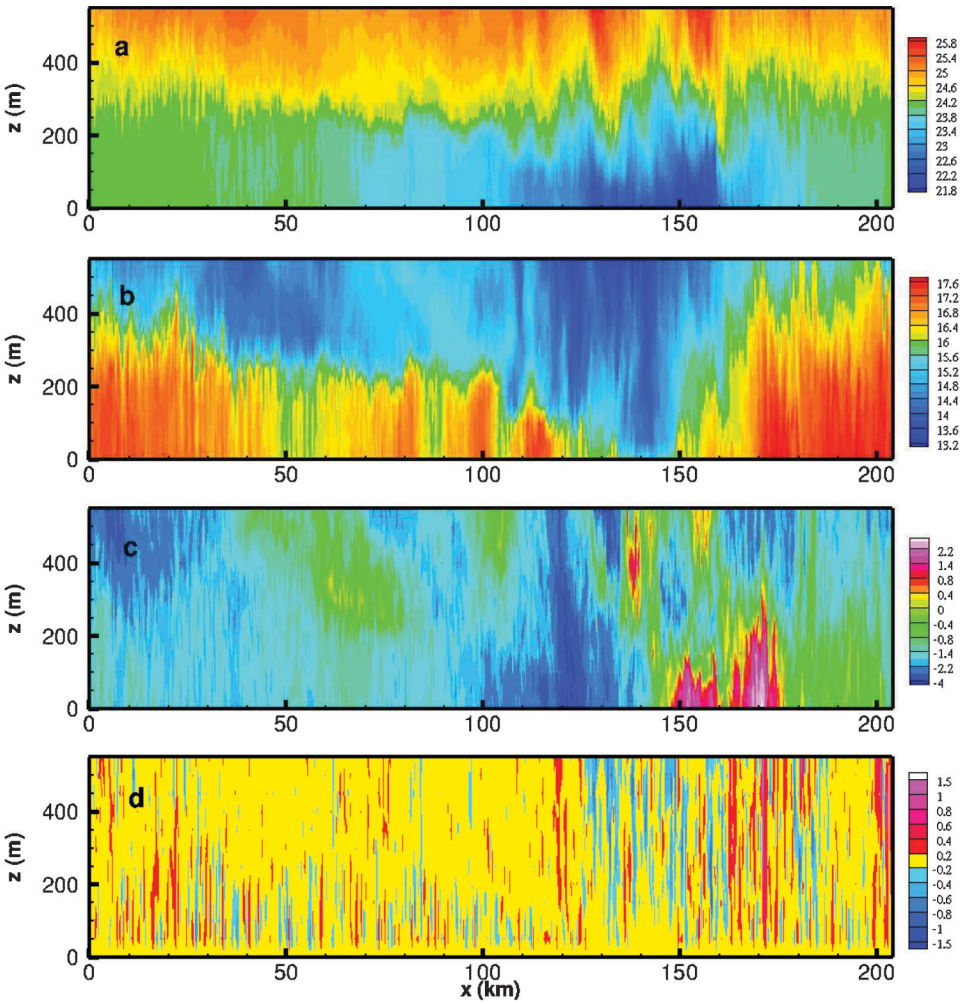

Figure 3. Vertical cross-sections of (a) potential temperature (degree C), (b) water vapor mixing ratio (g kg^{-1}), (c) u-velocity (m s^{-1}), and (d) w-velocity (m s^{-1}) along y= 90 km, from the LES.

12 hours of simulation, below 2 km. If we arbitrarily define the mean cloud base at the height where the horizontal mean cloud water mixing ratio reaches 0.01 g kg^{-1} (contour colors change from blue to yellow), then the mean cloud base is about 600 m. The TKE plot suggests that the mean PBL depth stays around 250 m. Figures 5 and 6 also suggest that the mean PBL height is around 250 m where the mean potential temperature inside and outside the cold pool merge and where the horizontal-mean heat flux shows a minimum.

To see if the statistics within the selected 20 km × 20 km subdomains are representive of the inside and outside cold pool regions, we performed another conditional sampling where the cold-pool subdomain consists of all grid points where the near-surface potential temperature (of Fig. 2a) is 1 K below the horizontal mean and the outside-cold-pool subdomain includes all grid points where the near-surface potential temperature is 0.5 K above the mean. Their mean and flux profiles (not shown) behave similarly to those shown in Figs. 5 and 6.

The above description of cold pools is not unique from the LES. A CRM with a grid size of few kilometers can also capture this phenomenon reasonably well (e.g., Trier et al. 1996) because cold pools are cloud-system scale. What's unique about this LES is that it also resolves large energy-containing turbulent eddies, while coarse-grid CRMs don't. Thus the LES can be used to study the relationship between the turbulence and the cloud-system scales. But first we will show the range of scales that are resolved in this LES by performing a spectral analysis.

3. Spectral analysis

The power spectra and the co-spectra of the vertical velocity w and the water vapor mixing ratio q at z=150 m and 1.2 km (as examples) are plotted against the wavenumber in the x direction ($n_x \equiv L_x \lambda^{-1}$, where λ is the wavelength and L_x is the total numerical domain size in x) as solid curves in Fig. 8. (The non-solid curves show low-pass filtered spectra, which will be described in section 4.) These spectra were

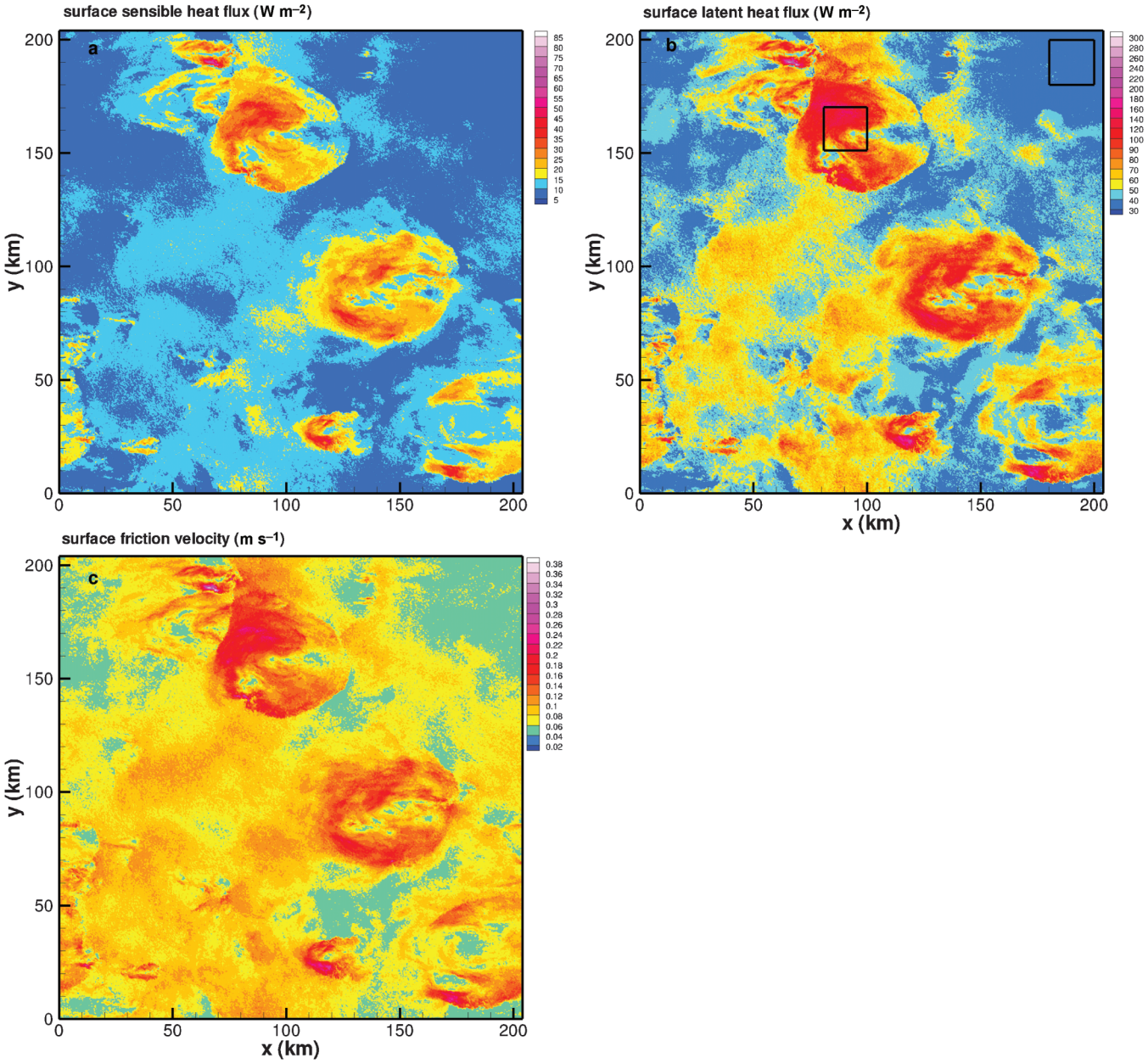

Figure 4. Horizontal distributions of surface temperature flux, latent heat flux, and friction velocity. The two boxes in Fig. b represent two reference subdomains for inside and outside of cold pools.

computed by performing 2D FFT over the horizontal plane and then averaging along the y-wavenumber space. The coordinates in Fig. 8 are chosen such that the areas covered under these curves represent the variances and the co-variances (i.e., vertical fluxes) of the variables. For the numerical domain simulated here, n_x= 1, 10, 100, 1000 correspond to wavelengths of about 200 km, 20 km, 2 km, and 200 m, respectively. At z = 150 m (blue curves), most of the *w*-variance reside at scales smaller than about 2 km (i.e., $n_x > 100$), while most of the *q*-variance reside at the cold-pool scale ($\lambda > 20$ km or $n_x < 10$). Higher up, at z=1.2 km (red curves), the *w*-spectrum multiplied by n_x spreads out over a broad range of scales—from ~ 400 m (turbulence) all the way up to ~ 20 km (cloud system). The *q*-variance again concentrates on scales larger than $n_x \sim 30$ (or $\lambda \sim 7$ km).

At z = 150 m the *w*-*q* co-spectrum (multiplied by n_x) reveals two peaks: one at the turbulence scale and the other at the cold-pool scale. The turbulence and the cold-pool scales contribute about the same to the total moisture flux. A dip of this co-spectrum appears at scales between 4 to 10 kilometers, which separate the two major contributors of the

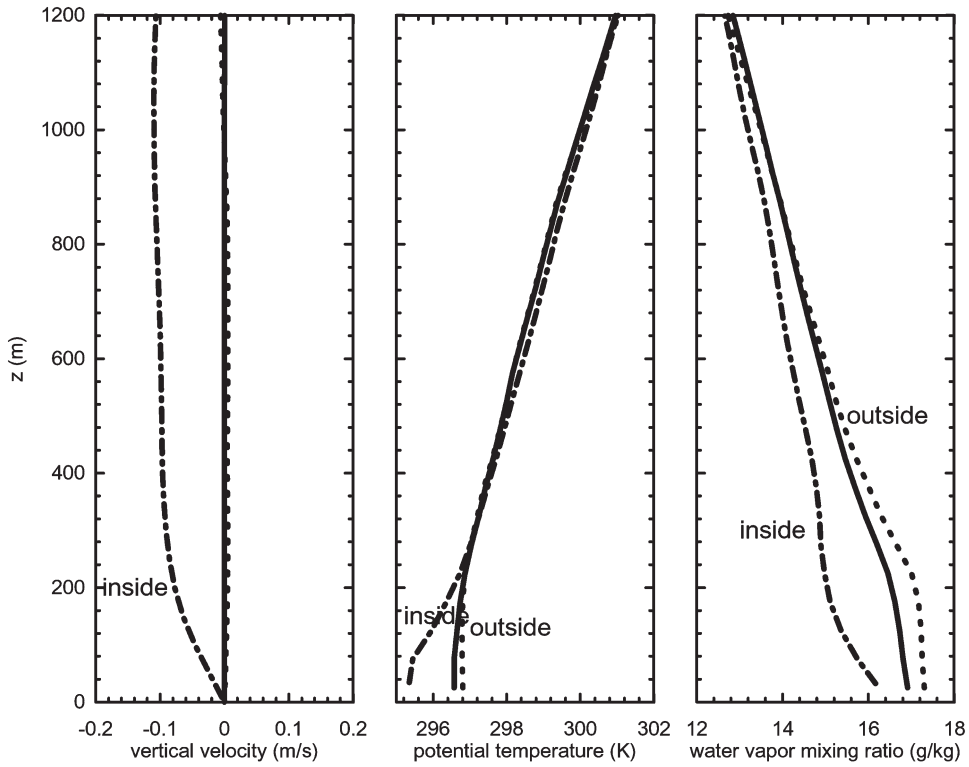

Figure 5. Vertical profiles of the mean vertical velocity, mean potential temperature and mean water vapor mixing ratio, averaged over the entire numerical domain (solid curves), cold-pool subdomain (dash-dot) and outside-cold-pool subdomain (dotted curves).

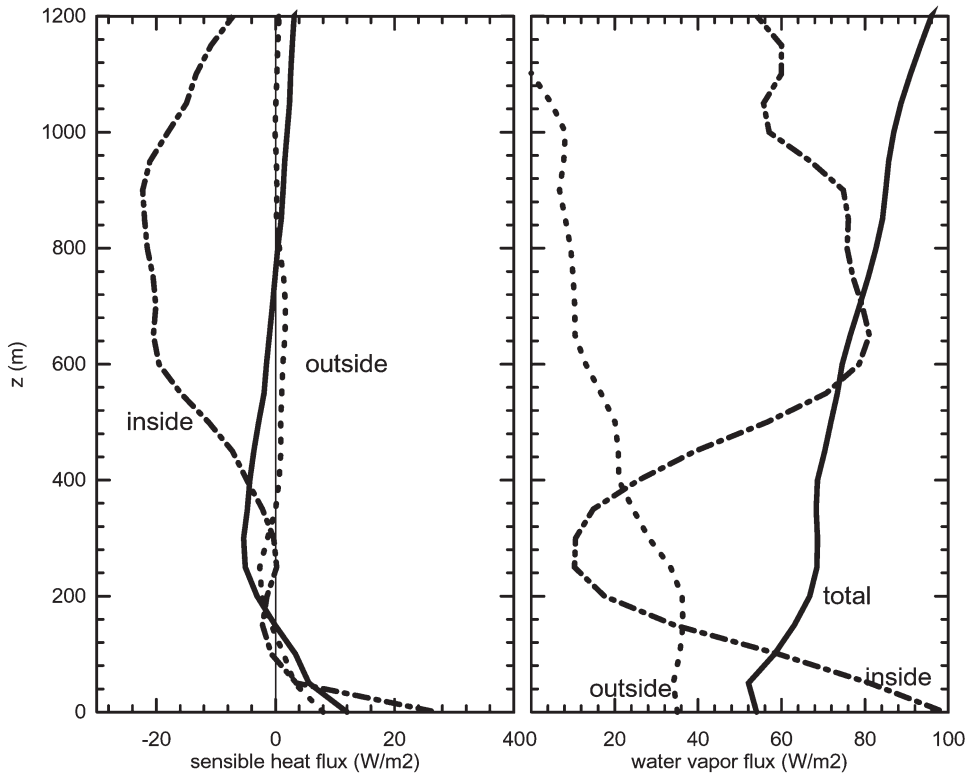

Figure 6. Vertical profiles of the vertical fluxes of potential temperature and water vapor mixing ratio, averaged over the entire numerical domain (solid curves), cold-pool subdomain (dash-dot curves) and outside-cold-pool subdomain (dotted curves).

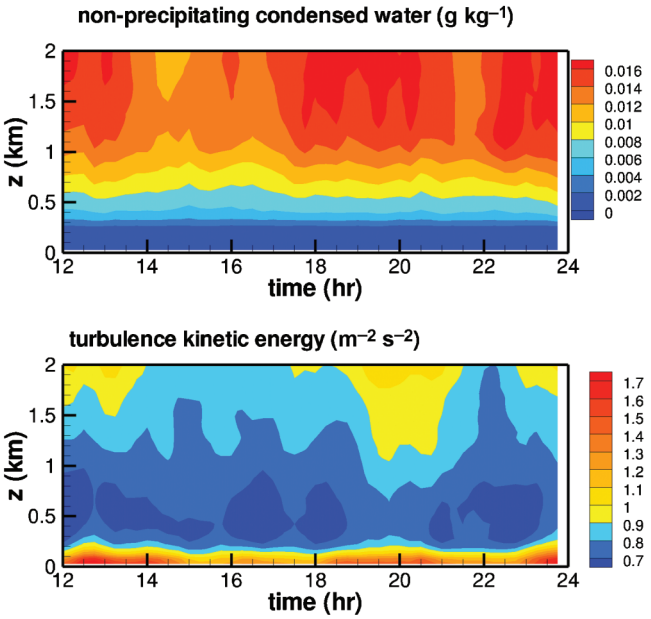

Figure 7. Contour plots of the non-precipitating condensed water and the turbulence kinetic energy below 2 km during the last 12 hours of simulation.

moisture flux in the PBL. (We do not show the sensible heat and momentum fluxes because they are both negligibly small in the PBL since the surface-air temperature difference and the near-surface mean wind are both small in this selected case.)

However, at z = 1.2 km, the *w*-*q* cospectrum multiplied by n_x is flat over a broad range of scales (from several hundreds of meters to several tens of kilometers) suggesting that all convection scales are important contributors to the moisture flux in the lower-cloud layer. We examined the spectra and co-spectra at all levels and found that the dip in the *w*-*q* co-spectrum exists only below z∼700 m. The co-spectral dip shown in Fig. 8 disappears higher up into the lower cloud layer. Figure 7 suggests that 700 m may be the base of all convective cloud types.

As elaborated in next section, the spectra that are filtered by a Gaussian 2D (*x*-*y*) filter with a width of 1 km (shown as dotted curves in Fig. 8) effectively eliminates most of the *w*-variance at this height, as well as the turbulence contribution to the moisture flux. Hence, in this study we loosely define "turbulence" as scales that are filtered out by a filter width of 1 km.

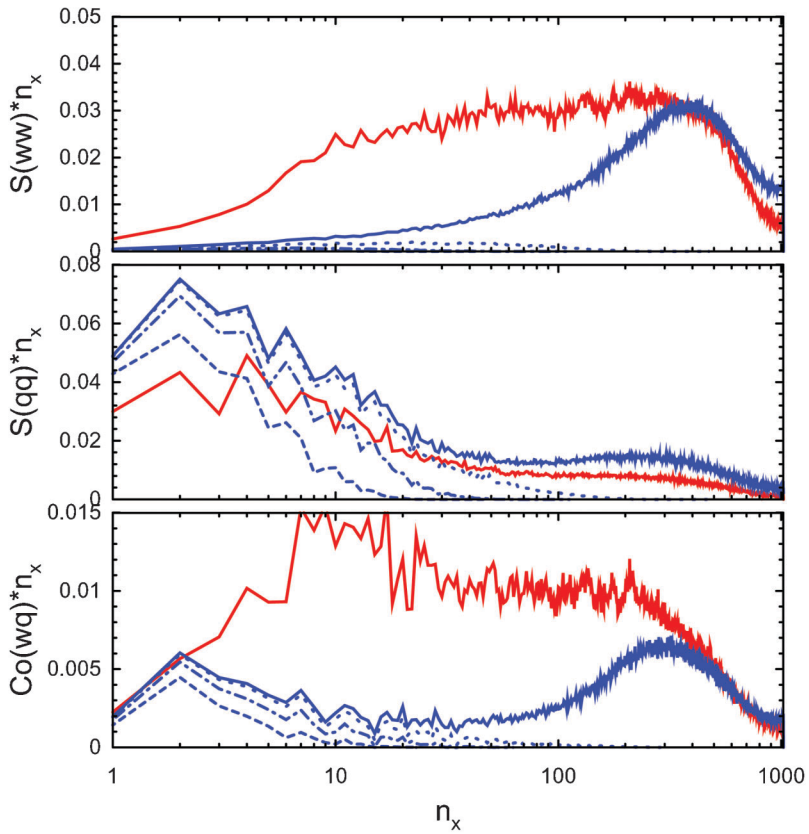

Figure 8. Power spectra of vertical velocity, water vapor mixing ratio, and their co-spectrum (all multiplied by n_x) at z = 150m (blue) and z = 1.2 km (red). The solid curves are from the unfiltered LES field while the non-solid curves are the filtered fields with various filter widths (dotted curves: Δ_f=1km; dash-dot: Δ_f=4km; dashed: Δ_f =10km). The units of *S*(*ww*), *S*(*qq*) and *S*(*wq*) are the same as those of *w*-variance, *q*-variance and *w*-*q*-covariance, respectively.

4. Scale separation

We now use a Gaussian filter to decompose the scale of motions that are resolved in the LES into the filter-scale (FS) and the subfilter-scale (SFS). [A Gaussian filter is chosen for two reasons: first, it behaves similarly to a top-hat filter, which is implicitly used in a finite-differencing numerical model (Leonard 1974, Horst et al. 2004), and second, it does not generate numerical noise near the cutoff scale like the sharp-wave-cutoff filter does.] The FS (representing the cloud-system-scale) variable ($\tilde{c}$) is defined as

$$\tilde{c} = \int\int cG(x, y)\,dxdy, \tag{4.1}$$

where

$$G(x, y) = \frac{6}{\pi\Delta_f^2} e^{-6(x^2+y^2)/\Delta_f^2}, \tag{4.2}$$

and the SFS (representing the turbulence and small convection scales) variable as $c'' = c - \tilde{c}$. Tong et al. (1998) showed that 2D filtering in x and y is a good approximation of 3D volume filtering.

The filter width Δ_f can be viewed as a CRM's grid resolution, which is typically 4~6 times of the horizontal grid spacing due to truncation errors. Hence the FS can serve as a surrogate for the resolvable scales of a CRM with a grid resolution of Δ_f and the SFS serves as a surrogate for the SGS of a CRM. The cool pools described earlier are resolvable scales in a typical CRM, while turbulence and small clouds belong to SFS.

We apply the Gaussian filter to the simulated w and q fields at z = 150 m with Δ_f = 1 km, 4 km and 10 km, respectively, and show the filtered spectra and co-spectra in Fig. 8 (the non-solid blue curves). The smaller-scale contributions to the variances and the covariance are progressively filtered out as expected. With a filter width of 1 km, most of the w-variance is eliminated at this height, implying that a CRM with this grid resolution barely resolves any vertical-velocity fluctuations at this height. Note that for one-dimensional spectra in n_x shown here, a significant reduction in variances and covariances occurs even at low wavenumbers due to the filtering along n_y. At z=150 m, the filtering procedure with Δ_f=1 km effectively filters out the turbulence contribution to the total moisture flux.

The vertical profiles of the horizontally averaged moisture flux before (black curve) and after filtering (blue curves) are compared in Fig. 9. As anticipated, the moisture flux is progressively reduced with the increase of Δ_f. However, even in the lower layer, say z ~ 200 m, scales larger than turbulence (i.e., the resolvable scales with Δ_f = 1 km) are responsible for more than half of the total moisture transport.

In Fig. 9 we also plot the SFS fluxes (red curves), which are the difference between the total and the FS fluxes. The turbulent motion (the SFS with Δ_f= 1 km) is responsible for a significant portion of the moisture transport only near the surface; its contribution decreases with height to about 300 m and remains at about one-third of the total flux in the lower cloud layer.

Above we showed the horizontally averaged SFS fluxes and their dependence on filter width. However, to evaluate or develop SGS parameterizations for CRMs, we need to look beyond the horizontally averaged SFS fluxes. The key is the local relationship between the SFS fluxes and the resolvable FS motions.

5. Studying subgrid-scale representations in CRMs

The horizontally averaged SFS moisture fluxes shown as red curves in Fig. 9 are not the SGS fluxes that appear explicitly in the governing equations of CRMs. What's needed in every grid volume of a CRM are the local SGS fluxes, which appear in the volume filtered Navier-Stokes equation as

$$\tau_{wc} = \widetilde{wc} - \tilde{w}\,\tilde{c}, \tag{5.1}$$

where the tilde represents the grid-volume average and $\tilde{w}$ and $\tilde{c}$ are resolvable-scale variables in CRMs. [Equation 5.1 can be further expanded to include the cross terms and the Reynolds terms, but Eq. 5.1 is the general definition of SGS fluxes (e.g., Sullivan et al. 2003).]

The problem of SGS parameterization is to relate local SGS fluxes τ_{wc} to resolvable-scale variables (such as $\tilde{w}$ and $\tilde{c}$) at every grid point of a CRM. We will first compute the local

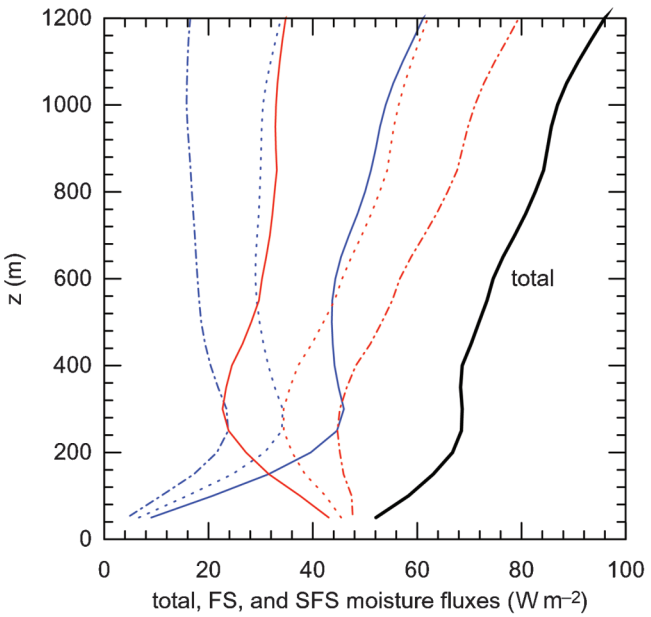

Figure 9. Vertical profiles of the horizontal means of the vertical q-fluxes before and after filtering with various filter widths (thin-solid curves: Δ_f = 1 km, i.e., the red solid curve; dotted curves: Δ_f = 4 km; dash-dot curves: Δ_f = 10 km). The total flux is shown in black, FS fluxes in blue, and SFS fluxes in red.

distributions of the SFS fluxes from the LES and then use the FS and the SFS fields to examine the relationship between resolvable field and SGS fluxes in CRMs. We will use the vertical flux of water vapor τ_{wq} as an example.

5.1. Horizontal distributions of the subfilter-scale moisture flux retrieved from LES

To retrieve the SFS vertical fluxes of water vapor, we apply Eqs. 4.1, 4.2 and 5.1 to the LES's w and q fields using various filter widths. The horizontal distributions of such retrieved τ_{wq} at $z = 200$ m and 600 m from $\Delta_f = 4$km, as examples, are shown in Fig. 10. (The horizontal averages of these τ_{wq} should be the same as those shown as red curves in Fig. 9.)

The SFS q-fluxes fluctuate widely in space, with local minimum and maximum values around -200 Wm^{-2} and 1350 Wm^{-2} at z=200m and about -270 Wm^{-2} and 3000 Wm^{-2} at z=600m. The horizontal averages over the whole numerical domain remain positive at about 36 and 45 Wm^{-2} at these two heights. At z=200 m, the local SFS fluxes tend to be negative inside cold pools and positive in the surroundings of cold pools. The positive SFS fluxes surrounding the cold pools increase in magnitude with height, and become significantly large at z = 600 m; these positive SFS fluxes occur at the outflow edges of cold pools (see Fig. 2c).

Using the retrieved SFS fluxes, we can evaluate existing SGS models in CRMs. In this study we examine a simple eddy diffusivity model.

5.2. Evaluation of an eddy diffusivity model

Many CRMs adopt the eddy diffusivity (K-model) approach to estimate the SGS fluxes. One commonly used scheme is to express the vertical SGS moisture flux as

$$\tau_{wq} = -K\frac{\partial \tilde{q}}{\partial z}, \tag{5.2}$$

with the eddy diffusivity K as

$$K = 0.1\ell\sqrt{e}, \tag{5.3}$$

following Deardorff (1980), where ℓ is a SGS length scale and e is the SGS TKE in a CRM.

From the LES database, we can compute all of the right-hand-side variables in Eqs. 5.2 and 5.3 except the length scale ℓ. In SAM (the CSU's System for Atmospheric Model), ℓ is set to its vertical grid size Δz. Applying $\ell = 50$m (which is the vertical grid size of the LES in the lowest 1 km) to Eq. 5.3 yields a horizontally averaged τ_{wq} that is too small by a factor of four compared to that shown in Fig. 9. So we empirically set $\ell = 200$ m.

The modeled τ_{wq} (from Eqs. 5.2 and 5.3) at $z = 200$ m and 600 m are presented in Fig. 11 and compared to those derived from the LES (shown in Fig. 10 using $\Delta_f = 4$ km as an example). At z=200 m, the K model predicts some

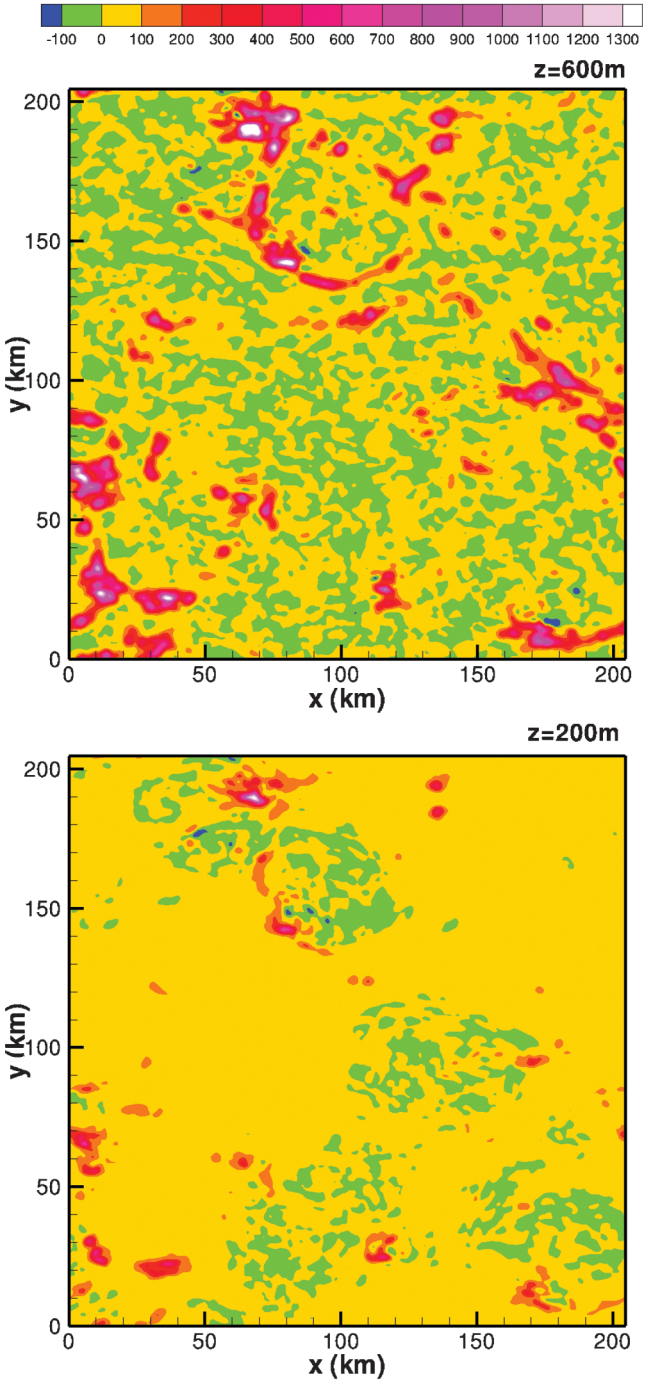

Figure 10. Horizontal distribution of the SFS flux of water vapor retrieved from the LES with a filter width of 4 km at (a) z = 600 m (top) and (b) z=200 m (bottom).

negative SGS fluxes in the cold pool areas which agrees with the LES diagnosis; however, it underpredicts the area coverages with negative fluxes. The local minimum and maximum in Fig. 11b are about -520 Wm^{-2} and 950 Wm^{-2}, respectively, compared to about -200 Wm^{-2} and 1350 Wm^{-2} diagnosed from the LES. Thus, the eddy diffusivity model overpredicts the negative fluxes but under-

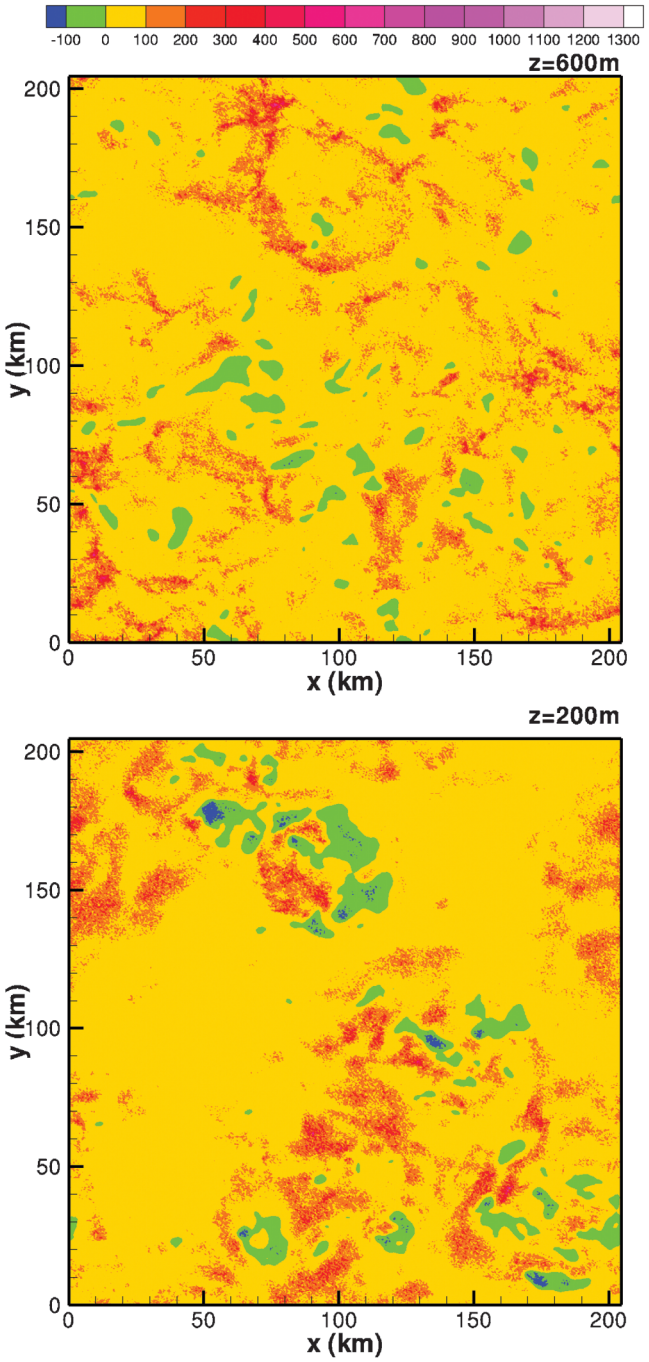

Figure 11. Horizontal distribution of the SFS flux of water vapor predicted from the K model using $\tilde{q}$ and SGS TKE from the LES fields, at (a) z = 600 m (top) and (b) z=200 m (bottom).

predicts the local maximum. At z = 600m, the K model also predicts well the positive SGS fluxes at the outer edges of the cold pools, but the magnitudes are largely underestimated. The local maximum in Fig. 11a is only about 860 Wm^{-2}, compared to about 3000 Wm^{-2} in Fig. 10a. There is no systematic bias in the model prediction.

To evaluate the model performance statistically, we compute the correlation coefficients between the modeled and

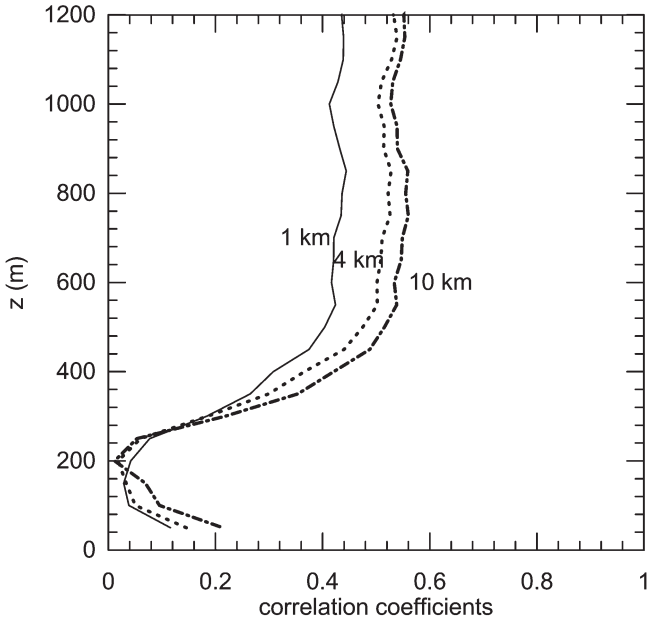

Figure 12. Vertical profiles of the correlation coefficients between the modeled and the LES-diagnosed SFS fluxes with various filter scales.

the LES-diagnosed SFS fluxes at all heights (but limited to 1.2 km in this study) for all three filter widths. The correlation coefficients (Fig. 12) are small, less than 0.2 below ~300 m but increase to about 0.5 above 400 m. This suggests that the K-model performs better in the lower-cloud layer than in the PBL. We checked these correlation coefficients at different time periods of the LES simulation and found similar results. The small correlation coefficients below ~ 300 m may be due to the fact that turbulence is not well resolved in the LES with its horizontal grid size of 100 m. But this does not explain the fact that the minimum correlation occurs at z ~ 200 m, rather than at lower levels.

An obvious defect of the K model is its independence of the CRM grid resolution if ℓ is set to the vertical grid size; Fig. 9 indicates that the horizontally averaged SFS fluxes should increase with the filter widths. But changing the specification of ℓ alone cannot improve the correlation coefficients because ℓ is usually assumed to be uniform horizontally. This shows a limitation of using the K model in representing the SGS effect in CRMs.

In the near future, we will investigate the differences between the LES-retrieved and K-modeled SGS flux distributions (Figs. 10 and 11) to see if the deficiencies of the K-model are related to surface fluxes, precipitation, local stability, resolved-scale vertical velocity, or local SGS TKE. Their relationships may provide clues for improving this K-model. We also plan to test more sophisticated schemes, such as higher-order closure schemes, mass-flux modeling, the assumed probability-density-function methods, or combinations of the above methods.

6. Summary and conclusions

As part of the CMMAP project, we performed a large-domain LES of a tropical deep convection system. This benchmark simulation has 2048 × 2048 × 256 grid points covering a tropical oceanic domain of about 205 km × 205 km × 27 km. The solution is used to study the relationship between the SGS processes and the resolvable cloud-system scales in CRMs.

In this study, we focused on the lowest kilometer of the simulated convective system, which includes the PBL and the lower cloud layer. We first showed that the PBL is highly heterogeneous and dominated by convection-induced cold pools, and that the cold-pool properties agree reasonably well with field observations. We performed a spectral analysis and showed that the vertical-velocity fluctuations reside mostly at turbulence scales while the moisture fluctuations at cloud system (cold-pool) scales. However, their co-spectrum (multiplied by the wavenumber) reveals two peaks at both turbulence and cloud-system scales with a clear spectral dip in between. This is true in the PBL. Higher up, above z ~ 700 m, the co-spectral dip disappears; convection and turbulence of all scales play important roles to the vertical transport of moisture in the lower cloud layer.

We applied a Gaussian filter to separate the LES flow field into the FS and the SFS—to represent, respectively, the resolvable and the SGS in CRMs. We retrieved the local SFS fluxes from the LES, and used the decomposed flow fields to study the relationship between the resolvable and the SGS fluxes in CRMs. We used an eddy diffusivity SGS model as an example to show that the LES can serve as a useful database to evaluate, and further to improve, SGS parameterizations for CRMs.

We have not looked into the physical processes that couple the PBL and cumulus clouds. To study the PBL-cloud interaction, such as how convective downdrafts that enter the PBL modify the convective available potential energy or how the PBL air modifies the subsequent development of cumulus clouds, requires a detailed analysis of the time evolution of the whole LES flow field, which will be studied in the near future.

Acknowledgements: This material is based upon work supported by the National Science Foundation Science and Technology Center for Multi-Scale Modeling of Atmospheric Processes CMMAP, managed by Colorado State University under cooperative agreement No. ATM-0425247. National Center for Atmospheric Research is sponsored by the NSF. The LES was performed using the IBM BlueGene/L "New York Blue" supercomputer at the New York Center for Computational Sciences, which is a joint venture of Stony Brook University and Brookhaven National Laboratory.

References

Barnes, G. M. and M. Garstang, 1982: Subcloud layer energetic of precipitating convection. *Mon. Wea. Rev.*, **110**, 102–117, doi: 10.1175/1520-0493(1982)110<0102:SLEOPC>2.0.CO;2.

Betts, A. K., 1976: The thermodynamic transformation of the tropical subcloud layer by precipitation and downdrafts. *J. Atmos. Sci.*, **33**, 1008–1020, doi: 10.1175/1520-0469(1976)033<1008:TTTOTT>2.0.CO;2.

Bryan, G. H., J. C. Wyngaard, and J. M. Fritsch, 2003: Resolution requirements for the simulation of deep moist convection. *Mon. Wea. Rev.*, **131**, 2394–2416, doi: 10.1175/1520-0493(2003)131<2394:RRFTSO>2.0.CO;2.

Fitzjarrald, D. R. and M. Garstang, 1981: Boundary-layer growth over the tropical ocean. *Mon. Wea. Rev.*, **109**, 1762–1771, doi: 10.1175/1520-0493(1981)109<1762:BLGOTT>2.0.CO;2.

Garstang, M. and A. K. Betts, 1974: A review of the tropical boundary layer and cumulus convection: structure, parameterization, and modeling. *Bull. Amer. Meteor. Soc.*, **55**, 1195–1205, doi: 10.1175/1520-0477(1974)055<1195:AROTTB>2.0.CO;2.

Geldmeier, M. F. and G. M. Barnes, 1997: The "footprint" under a decaying tropical mesoscale convective system. *Mon. Wea. Rev.*, **125**, 2879–2895, doi: 10.1175/1520-0493(1997)125<2879:TFUADT>2.0.CO;2.

Grabowski, W. W., X. Wu, M. W. Moncrieff, and W. D. Hall, 1998: Cloud-resolving modeling of cloud systems during Phase III of GATE. Part II: Effects of resolution and the third spatial dimension. *J. Atmos. Sci.*, **55**, 3264–3282, doi: 10.1175/1520-0469(1998)055<3264:CRMOCS>2.0.CO;2.

Horst, T. W., J. Kleissl, D. H. Lenschow, C. Meneveau, C.-H. Moeng, M. B. Parlange, P. P. Sullivan, and J. C. Weil, 2004: HATS: Field observations to obtain spatially filtered turbulence fields from crosswind arrays of sonic anemometers in the atmospheric surface layer. *J. Atmos. Sci.*, **61**, 1566–1581, doi: 10.1175/1520-0469(2004)061<1566:HFOTOS>2.0.CO;2.

Johnson, R. H., 1981: Large-scale effects of deep convection on the GATE tropical boundary layer. *J. Atmos. Sci.*, **38**, 2399–2413, doi: 10.1175/1520-0469(1981)038<2399:LSEODC>2.0.CO;2.

Johnson, R. H. and M. E. Nicholls, 1983: A composite analysis of the boundary layer accompanying a tropical squall line. *Mon. Wea. Rev.*, **111**, 308–319, doi: 10.1175/1520-0493(1983)111<0308:ACAOTB>2.0.CO;2.

Jorgensen, D. P., M. A. LeMone, and S. B. Trier, 1997: Structure and evolution of the 22 February 1993 TOGA-COARE squall line: aircraft observations of structure, circulation, and surface energy fluxes. *J. Atmos. Sci.*, **54**, 1961–1985, doi: 10.1175/1520-0469(1997)054<1961:SAEOTF>2.0.CO;2.

Khairoutdinov, M. F. and D. A. Randall, 2003: Cloud resolving modeling of the ARM summer 1997 IOP: Model formulation, results, uncertainties, and sensitivities. *J. Atmos. Sci.*, **60**, 607–625, doi: 10.1175/1520-0469(2003)060<0607:CRMOTA>2.0.CO;2.

Khairoutdinov, M. F. and D. A. Randall, 2006: High-resolution simulation of shallow-to-deep convection transition over land. *J. Atmos. Sci.*, **63**, 3421-3436, doi: 10.1175/JAS3810.1.

Khairoutdinov, M. F., S. K. Krueger, C.-H. Moeng, P. Bogenschutz, and D. A. Randall, 2009: Large-eddy simulation of maritime deep tropical convection. *J. Adv. Model. Earth Syst.*, **Vol. 1**, Art. #15, 13 pp., doi: 10.3894/JAMES.2009.1.15.

Klemp, J. B., and R. B. Wilhelmson, 1978: The simulation of three-dimensional convective storm dynamics. *J. Atmos. Sci.*, **35**, 1070–1096, doi: 10.1175/1520-0469(1978)035<1070:TSOTDC>2.0.CO;2.

Krueger, S. K. 1988: Numerical simulation of tropical cumulus clouds and their interaction with the subcloud layer. *J. Atmos. Sci.*, **45**, 2221–2250, doi: 10.1175/1520-0469(1988)045<2221:NSOTCC>2.0.CO;2.

Leonard, A. 1974: Energy cascade in large eddy simulations of turbulent fluid flows. *Advances in Geophysics*, **18**, *Academic Press*, 237–248.

Nicholls, M. E., and R. H. Johnson, 1984: A model of a tropical squall line boundary layer wake. *J. Atmos. Sci.*, **41**, 2774–2792, doi: 10.1175/1520-0469(1984)041<2774:AMOATS>2.0.CO;2.

Nicholls, S. and M. A. LeMone, 1980: The fair weather boundary layer in GATE: The relationship of subcloud fluxes and structure to the distribution and enhancement of cumulus clouds. *J. Atmos. Sci.*, **37**, 2051–2067, doi: 10.1175/1520-0469(1980)037<2051:TFWBLI>2.0.CO;2.

Redelsperger, J. L. and G. Sommeria, 1986: Three-dimensional simulation of a convective storm: Sensitivity studies on subgrid parameterization and spatial resolution. *J. Atmos. Sci.*, **43**, 2619–2635, doi: 10.1175/1520-0469(1986)043<2619:TDSOAC>2.0.CO;2.

Redelsperger, J. L. and co-authors, 2000: A GCSS model intercomparison for a tropical squall line observed during TOGA-COARE. Part I: Cloud-resolving models. *Quart. J. Roy. Meteor. Soc.*, **126**, 823–863, doi: 10.1256/smsqj.56403.

Sullivan, P. P., T. W. Horst, D. H. Lenschow, C.-H. Moeng and J. C. Weil, 2003: Structure of subfilter-scale fluxes in atmospheric surface layer with application to large-eddy simulation modelling. *J. Fluid Mech.*, **482**, 101–139, doi: 10.1017/S0022112003004099.

Tao, W.-K. and S.-T. Soong, 1986: A study of the response of deep tropical clouds to mesoscale processes: Three-dimensional numerical experiments. *J. Atmos. Sci.*, **43**, 2653–2676, doi: 10.1175/1520-0469(1986)043<2653:ASOTRO>2.0.CO;2.

Trier, S. B., W. C. Skamarock, M. A. LeMone, D. B. Parsons, and D. P. Jorgensen, 1996: Structure and evolution of the 22 February 1993 TOGA-COARE squall line: numerical simulations. *J. Atmos. Sci.*, **53**, 2861–2886, doi: 10.1175/1520-0469(1996)053<2861:SAEOTF>2.0.CO;2.

Tong, C. J. C. Wyngaard, S. Khanna, and J.G. Brasseur, 1998: Resolvable- and subgrid-scale measurement in the atmospheric surface layer: The technique and issues. *J. Atmos. Sci.*, **55**, 3114–3126, doi: 10.1175/1520-0469(1998)055<3114:RASSMI>2.0.CO;2.

Weisman, M. L., W. C. Skamarock, and J. B. Klemp, 1997: The resolution dependence of explicitly modeled convective systems. *Mon. Wea. Rev.*, **125**, 527–548, doi: 10.1175/1520-0493(1997)125<0527:TRDOEM>2.0.CO;2.

Williams, A. G., H. Kraus, and J. M. Hacker, 1996: Transport processes in the tropical warm pool boundary layer. Part I: Spectral composition of fluxes. *J. Atmos. Sci.*, **53**, 1187–1202, doi: 10.1175/1520-0469(1996)053<1187:TPITTW>2.0.CO;2.

Young, G. S., S. M. Perugini, and C. W. Fairall, 1995: Convective wakes in the equatorial western Pacific during TOGA. *Mon. Wea. Rev.*, **123**, 110–123, doi: 10.1175/1520-0493(1995)123<0110:CWITEW>2.0.CO;2.

Zipser, E. J., 1969: The role of organized unsaturated convective downdrafts in the structure and rapid decay of an equatorial disturbance. *J. Appl. Meteor.*, **8**, 799–814, doi: 10.1175/1520-0450(1969)008<0799:TROOUC>2.0.CO;2.

Zipser, E. J., 1977: Mesoscale and convective-scale downdrafts as distinct components of squall-line structure. *Mon. Wea. Rev.*, **105**, 1568–1589, doi: 10.1175/1520-0493(1977)105<1568:MACDAD>2.0.CO;2.